Water Research 209 (2022) 117954

Contents lists available at ScienceDirect

Water Research

journal homepage: www.elsevier.com/locate/watres

Nanobubble-assisted scaling inhibition in membrane distillation for the treatment of high-salinity brine

Muhammad Usman Farid [a,1], Jehad A. Kharraz [a,1], Cheng-Hao Lee [b,c], James Kar-Hei Fang [b,d,e], Sophie St-Hilaire [f], Alicia Kyoungjin An [a,*]

[a] School of Energy and Environment, City University of Hong Kong, at Chee Avenu, Kowloon, China Hong Kong Special Administrative Region
[b] Department of Applied Biology and Chemical Technology, The Hong Kong Polytechnic University, Kowloon, China Hong Kong Special Administrative Region
[c] Institute of Textiles and Clothing, The Hong Kong Polytechnic University, Kowloon, China Hong Kong Special Administrative Region
[d] Research Institute for Future Food, The Hong Kong Polytechnic University, Kowloon, China Hong Kong Special Administrative Region
[e] State Key Laboratory of Marine Pollution, City University of Hong Kong, Kowloon, China Hong Kong Special Administrative Region
[f] Department of Infectious Disease and Public Health, City University of Hong Kong, Kowloon, China Hong Kong Special Administrative Region

ARTICLE INFO

Keywords:
Membrane distillation
Nanobubbles
Scaling
Brine treatment
Hydrodynamic disturbance
Charge

ABSTRACT

In this study, we report the use of nanobubbles (NBs) as a simple and facile approach to effectively delay scaling in membrane distillation (MD) during the treatment of highly saline feed (100 g L^{-1}). Unlike conventional gas bubbling in MD for improving the hydrodynamic flow conditions in the feed channel, here we generated air NBs with an average size of 128.81 nm in the feed stream and examined their impact on membrane scaling inhibition during MD operation. Due to their small size, neutral buoyancy, and negative surface charge, NBs remain in suspension for a longer time (14 days), providing homogenous mixing throughout the entire feed water. The MD performance results revealed that severe membrane scaling happened during the DCMD treatment of high salinity brine in the absence of nanobubbles, which dramatically reduced the distillate flux to zero after 13 h. A one-time addition of air NBs in the saline feed significantly reduced salt precipitation and crystal deposition on the PVDF membrane surface, delayed the occurrence of flux decline, prevented membrane wetting, thereby prolonging the effective MD operating time. With similar feed concentration and operating conditions, only 63% flux decline after 98 h operation was recorded in nanobubble-assisted MD. Two key explanations were suggested for the delayed membrane scaling upon addition of air NBs in the MD feed: (1) NB-induced turbulent flow in the feed channel that increases the surface shear forces at the membrane surface, alleviating both temperature and concentration polarization effect, (2) electrostatic attractions of the counterions to the negatively charged NBs, which reduces the availability of these ions in the bulk feed for scale formation.

1. Introduction

Rapid urbanization, unprecedented population growth, and the increasing rate and magnitude of climate change have triggered severe freshwater crises, particularly in coastal and inland regions (Deshmukh et al., 2018). Thermally driven desalination technologies capable of treating high-salinity waters using low-grade heat sources, such as waste, solar, and geothermal heat, are vital in using the water-energy nexus to address these crises (Deshmukh et al., 2018). Membrane distillation (MD), a membrane/thermal hybrid process, has emerged as the treatment method of choice for desalinating high-salinity waters, such as sea and brackish water, saline wastewaters, and brines (Drioli et al., 2015; Kharraz et al., 2020; Pangarkar et al., 2016). MD possesses notable advantages over conventional thermal distillation and membrane separation processes, namely (1) its relative insensitivity to feed salinity;(2) its lack of specialized high-pressure requirements, unlike reverse osmosis; (3) its potential for 100% rejection of ions and macromolecules; and (4) its relatively low operation temperature requirement, increasing the feasibility of using renewable heating sources as the thermal driving force (Alkhudhiri et al., 2012; Deshmukh et al., 2018; Ullah et al., 2018). However, despite its many advantages, large-scale practical applications of MD for treating high-salinity water remain

* Corresponding author.
E-mail address: alicia.kjan@cityu.edu.hk (A.K. An).
[1] These authors contributed equally to this work.

https://doi.org/10.1016/j.watres.2021.117954
Received 6 July 2021; Received in revised form 4 December 2021; Accepted 6 December 2021
Available online 9 December 2021

limited. A major bottleneck in their widespread adoption is the inevitable scaling (i.e., inorganic fouling) of the MD membranes due to the precipitation of sparsely soluble salts present in the feed stream (Horseman et al., 2021; Rezaei et al., 2020; Tijing et al., 2015). Scaling in MD is particularly crucial, as this phenomenon increases heat and mass transfer resistance, escalates membrane wetting, and aggravates temperature and concentration polarization at the membrane surface, all of which deteriorate overall MD performance (Horseman et al., 2021; Rezaei et al., 2018; Warsinger et al., 2015).

Various techniques, such as feed water pretreatment (e.g., filtration, coagulation, antiscalant use), chemical cleaning (e.g., use of acids or bases), and membrane surface modification (e.g., altering the surface roughness, hydrophobicity, and surface charges) have been developed to control scaling in MD (Deka et al., 2019; Gryta, 2008a; Kamranvand et al., 2020; Kharraz et al., 2020; Zhang et al., 2015). However, these techniques prevent scaling only to a certain extent, and their use entails other environmental, economic, and operational concerns. For instance, most antiscalant chemicals are organics and may reduce the surface tension of the water, thereby promoting membrane wetting (He et al., 2009). In addition, some antiscalant chemicals (e.g., polyacrylate-based antiscalants), when added to the feed, serve as a nutritional source for bacteria and thus promote biofouling on the membrane surface (He et al., 2009; Sweity et al., 2013). Furthermore, the use of these chemicals can be an environmental concern because most antiscalants do not readily degrade in natural environments. Moreover, studies have reported contradictory results regarding superhydrophobic and omniphobic surface modification effects on anti-scaling performance (Liu et al., 2021). Hydrophobic surfaces are also known to preferentially adsorb organic compounds present in natural feed water, which may modify the membrane surface and thus facilitate scaling and membrane wetting (Eykens et al., 2017; Servi et al., 2016). Finally, pretreatment and MD process parameter optimization, which incur additional costs, have failed to eliminate scaling in MD ultimately.

Considering the severity of scaling in MD and the limitations of current technologies in addressing this problem, it is essential to seek a chemical-free approach that effectively prevents scaling and avoids environmental or operational damage. One practical physical approach to prevent scaling in MD during the treatment of high-salinity water is to create better fluid dynamics and increase the surface shear rate near the membrane surface. Conventionally, flow turbulence in the feed channel is stimulated by either increasing the feed flow velocity or using spacers. However, Chen et al. (2013) found that the use of spacers eventually leads to more scaling than in a configuration without spacers because spacers facilitate the local trapping of salts close to the membrane surface (). Another practical approach to increase shear stress near the membrane surface for membrane scaling control is the introduction of a gas-liquid two-phase flow via gas bubbling (Chen et al., 2013; Ding et al., 2011; Ye et al., 2019). Various studies have reported that bubbling-induced secondary flows significantly increase the maximum shear stress near the membrane surface, thus hindering local scale formation (Chen et al., 2013; Cui et al., 2003; Ye et al., 2019). Furthermore, when correctly used, bubble technology carries no risk of membrane damage and causes no harm to the environment. Studies have shown that the efficacy of bubble technology for fouling control in membrane-based systems is mainly dependent on the size and distribution of the produced bubbles, with uniformly distributed fine bubbles being more efficient in delaying membrane fouling than coarse bubbles under similar operation conditions (Chen et al., 2014; Cui et al., 2003).

The use of nanobubbles (NBs; tiny bubbles with a diameter of < 200 nm) is an alternative to the conventional bubbling technique, with great potential for scaling control in MD. NBs are incredibly small (500 times smaller than a microbubble) and stable cavities of gas in liquid and have unique physical characteristics, such as a large interfacial area, low or neutral buoyancy, long residence time, negative surface charge, and high internal pressure (Agarwal et al., 2011; Lugli et al., 2005). Compared with macro- and micro-bubbles, the neutral buoyancy and negative surface charge of NBs allow them to remain in the feed stream for relatively more extended periods (Bui et al., 2019; Ushikubo et al., 2010). For instance, microbubbles tend to gradually decrease in size and eventually collapse due to long stagnation and the dissolution of interior gases into the surrounding water, whereas NBs persist for months (Lugli et al., 2005; Ushikubo et al., 2010). Moreover, given their strong negative charge, NBs repel each other and thus thoroughly saturate the feed (Bui et al., 2019). The use of extremely small and uniformly distributed NBs in the MD feed stream is anticipated to increase the surface shear forces at the membrane surface significantly. These shear forces will disturb the boundary layer and reduce the chances of concentration polarization and scaling layer formation on the membrane surface. Moreover, the strong negative charge of NBs in the saline feed will effectively reduce salt precipitation, possibly by attracting counterions to the gas-water interface.

In this study, we investigated the influence of NB aeration as a chemical-free scale-inhibition technique for the MD treatment of high-salinity brine. During MD operation, nanosized air bubbles were added to the feed stream, and their effects on mass transfer, solute rejection, and membrane wetting were systematically examined.

2. Materials and methods

2.1. Materials and chemicals

A commercially available polyvinylidene fluoride (PVDF) membrane with a nominal pore size of 0.22 μm (GVHP Durapore) was purchased from Merck Millipore Ltd. USA and used as a standard hydrophobic MD membrane (hereafter referred to as C-PVDF). In each MD test, the membranes were used as obtained without any modifications. Sodium chloride (NaCl), magnesium sulfate ($MgSO_4$), sodium bicarbonate ($NaHCO_3$), and calcium chloride dihydrate ($CaCl_2{\cdot}2H_2O$) were used to prepare synthetic high-salinity feed solutions in either pristine or NB deionized (DI) water. $NaHCO_3$ and $CaCl_2{\cdot}2H_2O$ were purchased from Sigma-Aldrich Corporation, and $MgSO_4$ and NaCl were purchased from Dieckmann (Hong Kong) Chemical Industry Co., Ltd. Phenolphthalein was purchased from Sigma-Aldrich Corporation and used as an indicator during samples titration for the calculation of dissolved CO_2 concentrations. DI water with a resistivity of 18.3 MΩ was produced using a Milli-Q® water purification system (Merck Millipore) and used in all experiments. All salts used were of ACS reagent grade and were used as received.

2.2. Nanobubble Generation and characterization

NBs of natural air were generated for 15 min in 50 L acrylic tanks containing 20 L DI water using an NB generator (aQua+ 075MO, AquaPro Solutions Pte Ltd, Singapore). The pressure of the NB generator internal pump was controlled between 3.8 and 4.0 bar. Following the NB operation, the water in the tank was left undisturbed for 15 min.

The physiochemical characteristics of NBs, namely size (i.e., diameter), distribution, concentration, decay time, and zeta potential (ZP) in DI water, were characterized based on light scattering methods using nanoparticle tracking analysis (NTA, NanoSight LM10, and NanoSight NS300 systems, Malvern Panalytical Ltd, UK) and dynamic light scattering (DLS, ZEN3600 Zetasizer NanoZS, Malvern Instruments).

The NTA's NanoSight LM10 was used to measure the size and concentration of NBs over 30 min to 14 days, while the NanoSight NS300 was used to measure the concentration of NBs over a temperature range of 20–50°C. The systems utilize the properties of both light scattering and Brownian motion to obtain the size distribution and concentration measurement of particles in liquid suspension. A laser beam (blue laser with wave length $\lambda = 405$ nm) is passed through the sample chamber, and the NBs in suspension in the path of this beam scatter light in such a manner that they are easily visualized via a 20x magnification microscope onto which is mounted a high-speed camera. The camera operates

at 30 frames per second (fps), capturing a video file of the particles moving under Brownian motion. The software tracks many particles individually and calculates their hydrodynamic diameters using the Stokes-Einstein equation (Malvern Panalytical Ltd, 2021). After NBs generation and resting for 15 min as described above, six samples (each containing 50 mL of bubbled water) were collected from the tank at different time intervals (t_0 = initial, t_1 = 30 min, t_2 = 1 h, t_3 = 6 h, t_4 = 24 h, t_5 = 7 days, and t_6 = 14 days), and the characteristics of the NBs in the samples were analyzed, with three replicate measurements for each sample. DI water sampled before NB generation was used as the baseline standard. The effect of temperature variation on the concentration of NBs was also measured. In these temperature-dependence tests, the camera was operated at 25 fps with level = 10, gain = 73, and viscosity for water at 25°C = 0.9 cP. 1 mL of the NBs water was placed inside the testing chamber. The measuring temperature was automatically controlled at an accuracy of $\leq \pm 0.2$ °C by setting the desired value in the instrument's software before starting each test. The same sample was used during the testing temperature range (20–50°C) and was first stabilized at room temperature. Afterward, the temperature was set to 20°C to perform the first measurement, followed by increasing the temperature by steps of 10°C for the remaining tests. After the instrument reached the set temperature for each test, the sample was given 3 min to stabilize and reach thermal equilibrium before the test started.

The DLS's Zetasizer NanoZS was used to measure the size and size distribution of NBs over a temperature range of 20–70°C. The instrument uses non-invasive back scatter technology and has a detection range for diameters between 0.3 nm and 10 μm. The scattering angle was set to 173°, while the dispersant's (DI water) and material's (air NBs) refractive index (RI) was set to 1.33 and 1.0, respectively. Precautions were taken during the preparation and handling of samples to ensure no bubbles were formed during sample filling. 1 mL of the NBs water was filled in a disposable glass sizing cuvette and placed inside the testing chamber. The measuring temperature was automatically controlled at an accuracy of $\leq \pm 0.3$°C by setting the desired value in the instrument's software before starting each test. The same sample was used during the testing temperature range (20–70°C) and was first stabilized at room temperature for 15 min. Afterward, the temperature was reduced to 20°C to perform the first measurement, followed by increasing the temperature by steps of 10°C for the remaining tests. After the instrument reached the set temperature for each test, the sample was given 10–15 min to stabilize before the test started. Three replicate measurements were performed for each test with at least 13 runs each, and the mean value was reported.

Electrophoretic light scattering technology was used to measure the ZP of NBs water over a temperature range of 20–70°C using the same Zetasizer NanoZS described above. An electric field is applied to the NBs dispersion, leading the NBs to move. The velocity of the NBs is related to their ZP, which is measured using the laser interferometric technique (phase analysis light scattering M3-PALS technology). This enables the calculation of electrophoretic mobility, which is used to calculate the zeta potential based on the Smoluchowski equation. 1 mL of the NBs water was filled in a disposable folded capillary cell using the manufacturer-suggested procedure to ensure no air bubbles form in the cell. The same value and method for the refractive index and temperature control were applied, respectively, as mentioned in the size measurement section above. Three replicate measurements were performed for each test, and the mean value was reported. For both size and ZP and before the analysis of NBs, a transfer standard of latex nanospheres aqueous suspension was used to verify the correct operation of the Zetasizer NanoZS instrument.

The pH and conductivity of the DI water and NBs water were measured at room temperature using pre-calibrated pH and conductivity sensors connected to a digital meter (Multi 3420, WTW GmbH, Germany).

The concentration of dissolved CO_2 in two water samples: a control DI water and NBs-DI water, was measured by a titration reaction. Briefly, 10 mL of each sample was placed in a conical flask, and 2–3 drops of phenolphthalein indicator (0.25% solution in 60% ethyl alcohol) were added, after which the samples remained colorless, indicating to be acidic with the possible presence of free CO_2. This was followed by titrating the samples with 0.05 N NaOH solution until a pink color appeared, indicating the reaction's completion. This is due to the reaction of CO_2 with NaOH forming Sodium Bicarbonate, $NaHCO_3$ and turning the sample to become basic at around pH 8.3. At this completion point, based on the sample volume, and normality and volume of NaOH used, the concentration of CO_2 was calculated.

2.3. Membrane characterization

The surface morphology of both pristine and fouled membrane samples was evaluated using a field-emission scanning electron microscope (FE-SEM; Quanta FEG 450, FEI). SEM samples were initially gold-coated for 120 s (BTT-IV, Denton Vacuum, LLC, Moorestown, NJ, US). Elemental analysis of post-MD membranes (i.e., scaled samples) was performed via energy-dispersive spectroscopy (EDS) to identify the salt deposits.

The water contact angle (WCA) of the pristine and post-MD membranes was measured using a drop shape analyzer (DSA25, Kruss, Germany) and the double sessile drop measurement method with a 1 μL water droplet. At least two samples, with five readings each, were measured for each membrane. The membrane surface's zeta potential (ZP) was measured according to the streaming current technique by using a streaming potential analyzer (SurPASS, Anton Paar, Austria) equipped with an adjustable gap cell.

The bubble point (BP) (i.e., maximum pore size), mean flow pore size (MPS), minimum pore size, and average pore size distribution (PSD) were measured using a gas-liquid displacement porometer (Porolux™1000, Porometer, Belgium) and the wet/dry curve procedure. The membrane samples were pre-wetted using porefill (16 mN/m surface tension) and placed in the porometer chamber, where precise step-wise N_2 gas pressure was applied. The same porometer was operated under the hydro-head mode to measure all samples' water liquid entry pressure (LEP). LEP was recorded as the point at which a pressure increase was automatically detected, corresponding to the wetting of the largest pore through the water passage. The porosity of the membranes was measured as the difference between the dry and wetted sample weights (Eq. (1)) using a gravimetric method with butanol (0.81 g/mL) as the wetting liquid.

$$\varepsilon = \frac{W_{wet} - W_{dry}}{\rho_{Butanol} \times V_s} \quad (1)$$

where W_{wet} and W_{dry} are the wet and dry sample weights, respectively; $\rho_{Butanol}$ is the density of butanol, and V_s is the sample volume. A precision micrometer was used to measure the sample thickness.

The zeta potential of the membrane was measured using the same Zetasizer NanoZS instrument with an additional accessory, i.e., the surface zeta potential measurement cell that enables the measurement of the ZP of surfaces. Approximately 1 × 1 cm membrane sample was attached to the cell at the designated sample plate and submerged in a medium containing tracer particle (negatively charged). The surface ZP of the membrane is then determined by detecting the movement of tracer particles dispersed in the electrolyte in which the sample is immersed. An electric field is applied via the cell electrodes leading to a subsequent motion of tracer particle due to a combination of electrophoresis and electro-osmosis. Such movement is measured as a function of displacement away from the surface. The surface ZP is then calculated through a model that describes the electro-osmosis flow contribution from the sample surface.

2.4. Nanobubble-Membrane distillation setup and experiments

A lab-scale direct contact (DC) MD setup was used to evaluate the MD performance of all membranes Fig. 1. The setup consists of a 10 × 6 × 4 cm membrane module designed for an active flat-sheet membrane area of 6.2 × 1.5 cm, whose opposite sides are connected to two pumps circulating the feed and the permeate between the membrane module and the feed/permeate containers, respectively. The flowrates of the feed and the permeate were controlled using flowmeters connected beside the pumps. The temperature of the permeate and feed was controlled using a chiller maintained at 20 °C, and a hot plate maintained at 60 °C. This temperature difference of 40 °C between the two sides of the membrane drives the vapor through the hydrophobic membrane, following which the vapor condenses on the permeate side. Changes in permeate weight (used to calculate the vapor flux) and conductivity (used to calculate the salt rejection (SR)) are automatically recorded by a precision balance and a conductivity probe, respectively.

The same MD experimental setup was used to investigate the scale inhibition performance of NB-assisted MD in treating high-salinity water, with the only difference being the presence of NBs in the feed water. Briefly, in the NB-assisted MD test, NBs of natural air was first generated in a tank containing 20-L DI water for 15 min at a pressure of 4 bar. Next, 3-L bubbled DI water was collected from the tank. Salts were added in the concentrations indicated in Table 1 to prepare a synthetic high-salinity feed solution (hereafter referred to as HS-100) as the test feed (Fig. 1).

Three sets of DCMD experiments were designed to evaluate the performance of the C-PVDF membrane. The first set was designed to assess the effect of introducing only NBs on MD. Two feeds were prepared in DI water, with and without NBs. The second set was designed to evaluate the effectiveness of NBs in reducing membrane scaling propensity. Two feeds were prepared for this set, namely HS-100 in DI water and HS-100 in NB-DI water. In this second test, the experiment ran in a continuous mode without feed replenishment. The third set was performed to assess the benefits of NBs in long-term DCMD by using the HS-100 in NB-DI water as the test feed. In this third test, the experiment ran in a batch mode where the feed was replenished with DI water whenever 100 mL permeate was collected to keep the variation in feed concentration within 5%. DI water was used at the permeate side in all MD experiments, and the feed and permeate flowrates were maintained at 500 mL min^{-1}.

Table 1
Composition of the HS-100 synthetic brine feed.

Salt	Molarity (mM)	Concentration (g/L)
Calcium (Ca^{+2})	46.66	1.87
Magnesium (Mg^{+2})	107.00	2.60
Sodium (Na^{+})	1386.86	31.87
chloride (cl^{-})	1444.01	51.19
sulfate (as so_4^{-2})	106.81	10.26
Bicarbonate (HCO_3^{-})	35.90	2.19
pH at 25 °C	7.12	100 g/L
Conductivity at 25 °C (mS/μm)	112.8	

3. Results and discussion

3.1. Nanobubble water generation and characterization

Immediately after the nanobubble generator started, the DI water inside the tank turned into a milky appearance. This is due to the presence of a large number of micron-sized bubbles, which leaves the tank over a few minutes/seconds due to bursting either after rising to the surface (due to their buoyancy) or coalescing in the water solution (Atkinson et al., 2019). This was confirmed when the generator was stopped following 15 min of operation. The milky color disappears within a few minutes and becomes clear as the larger micron-sized bubbles burst out of the solution, leaving behind nanobubbles.

Because the generated NBs were too small to be visible to the naked

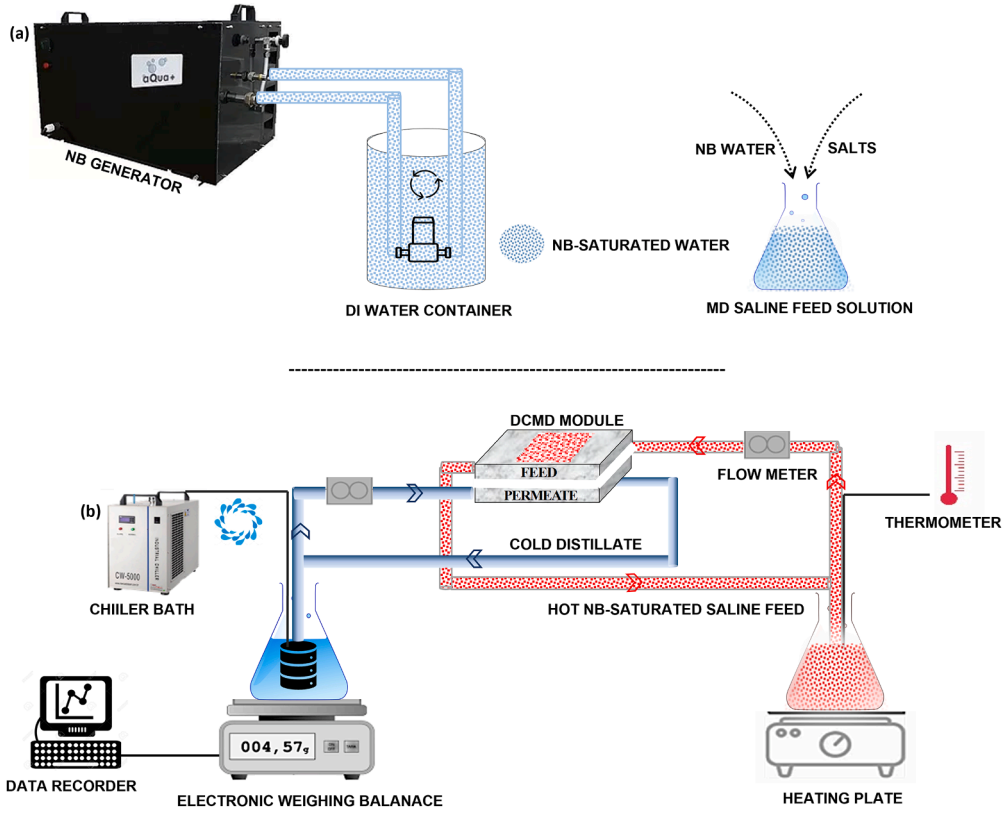

Fig. 1. Schematic diagram of (a) nanobubble (NB) generation and (b) direct contact membrane distillation (DCMD).

eye and even under a standard microscope (given their transparent nature), their presence in water was first visualized by the backscattering of light from a green laser pointer. As shown in Fig. 2A, the green laser beam was invisible in the beaker containing the control (ultrapure DI water without NBs). In contrast, it was visible in the beaker containing NB water. Note that the internal pump pressure of the NB generator showed an inverse relationship with bubble size. We optimized the generator pressure to 3.8–4 bar in the tests mentioned above to obtain small, uniformly distributed NBs.

It is well-established in the literature that NBs, once generated in the aqueous environment, remain highly stable for prolonged periods (Meegoda et al., 2018; Nirmalkar et al., 2018a; Ushikubo et al., 2010). To verify this, we further analyzed and quantified the fundamental characteristics of NBs, particularly their average bubble size, concentration, and stability, over 14 days by using NanoSight LM 10HS (see Section 2.2 for details) to observe changes in bubble size and concentration over time. The results showed that NBs generated with air in ultrapure DI water for 15 min yielded millions of NBs per mL, with each bubble measuring less than 150 nm in diameter (Fig. 2B and C). Specifically, the average bubble concentration was found to be approximately 7.8×10^7 bubbles mL^{-1}, with bubble diameters distributed in the narrow range of 100–150 nm. The size of the bubbles remained nearly unchanged over the 14 days, with an average bubble size of 142.81 nm on day 14, almost the same as that on day 1 (128.81 nm) (Fig. 2B). Similarly, the concentration of the NBs did not vary significantly, as only a 15% decrease in NB concentration was observed after 14 days (Fig. 2C).

The observed longevity of NBs in water, as evident from their consistent size and concentration for prolonged periods, can be attributed to the unique characteristics directly related to their nanoscale size, namely their high internal pressure, minimal buoyancy, and strong electric charge (Meegoda et al., 2018; Nirmalkar et al., 2018a). Unlike macro- or micro-bubbles, which quickly rise to and burst on the surface, the minimal buoyancy of NBs prevents them from reaching the surface; instead, they move around randomly following the principles of Brownian motion. The net effect is that NBs remain suspended in water for extended periods, moving randomly throughout the water suspension. Additionally, the electric charge on the NBs also plays an essential role in their stability (Nirmalkar et al., 2018a; Ushikubo et al., 2010). It is well-reported in the literature that air NBs formed in ultrapure water exhibit a high absolute negative ZP, which is attributed to the predominance of OH^- ions in the first molecular layers of water at the gas-liquid interface (Bui et al., 2019; Takahashi, 2005). We have measured the zeta potential of our NBs water as described in the methods section, and our results are in line with the reported literature showing a ZP value of 15.9 ± 2.7 mV at room temperature (i.e., 23°C) and pH of 6.8. The strong negative charge on the liquid-gas interface of NBs increases the degree of electrostatic repulsion between individual bubbles, thus keeping them evenly distributed in the water for longer, without coalescence.

Temperature is an essential parameter in all fields of natural science and has prominent effects on the physical and chemical properties of many materials and media and can affect their stability. The size and stability of macro-sized bubbles are also affected by the variation in temperatures due to a decreased gas solubility at higher temperatures. However, we expect a different behavior for NBs as they are fundamentally different and show high stability due to their unique characteristics, as explained above. Therefore, we have also tested the effect of temperature on physiochemical properties of the generated NBs water (Fig. 3). NBs were first generated at room temperature and left for 15 min after which a 1 mL sample was filled in a glass cell and placed in the sample chamber of either Zetasizer NanoZS or NanoSight LM10 instrument. The temperature was reduced to 20°C and left to stabilize for 10–15 min before starting the first test. This was followed by testing the size via increasing the temperature to 70°C and the concentration via increasing the temperature to 50°C. Fig. 3A and Fig. 3B show the intensity-weighted size distribution and average bubble diameter at a temperature range of 20°C–70°C, respectively. The NBs shows a relatively broad size range at low temperatures and become narrower with temperature increase. At lower temperatures (i.e., 20°C and 30°C) b, a wider range with two peaks could be seen. A move towards a single peak with narrower distribution is noticed at higher temperatures, confirming that NBs are temperature-sensitive (Fig. 3A). Measurement of NBs size (i.e., diameter) further confirms a larger NBs size at lower temperatures (154.93 ± 23.13 nm at 20°C) with a decreasing trend where the size shrinks to a minimum of 92.93 ± 13.12 nm at 40°C; the same

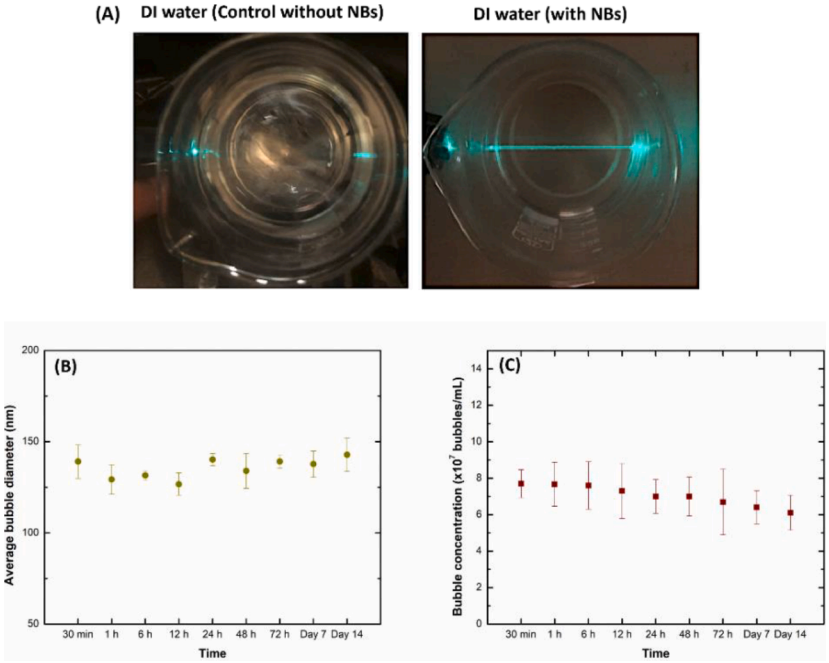

Fig. 2. Visualization and characteristics of nanobubbles in DI water. (A) absence and backscattering of light from a green laser pointer in DI water without NBs and DI water with NBs, respectively, and changes in (B) size and (C) concentration of NBs over 14 days.

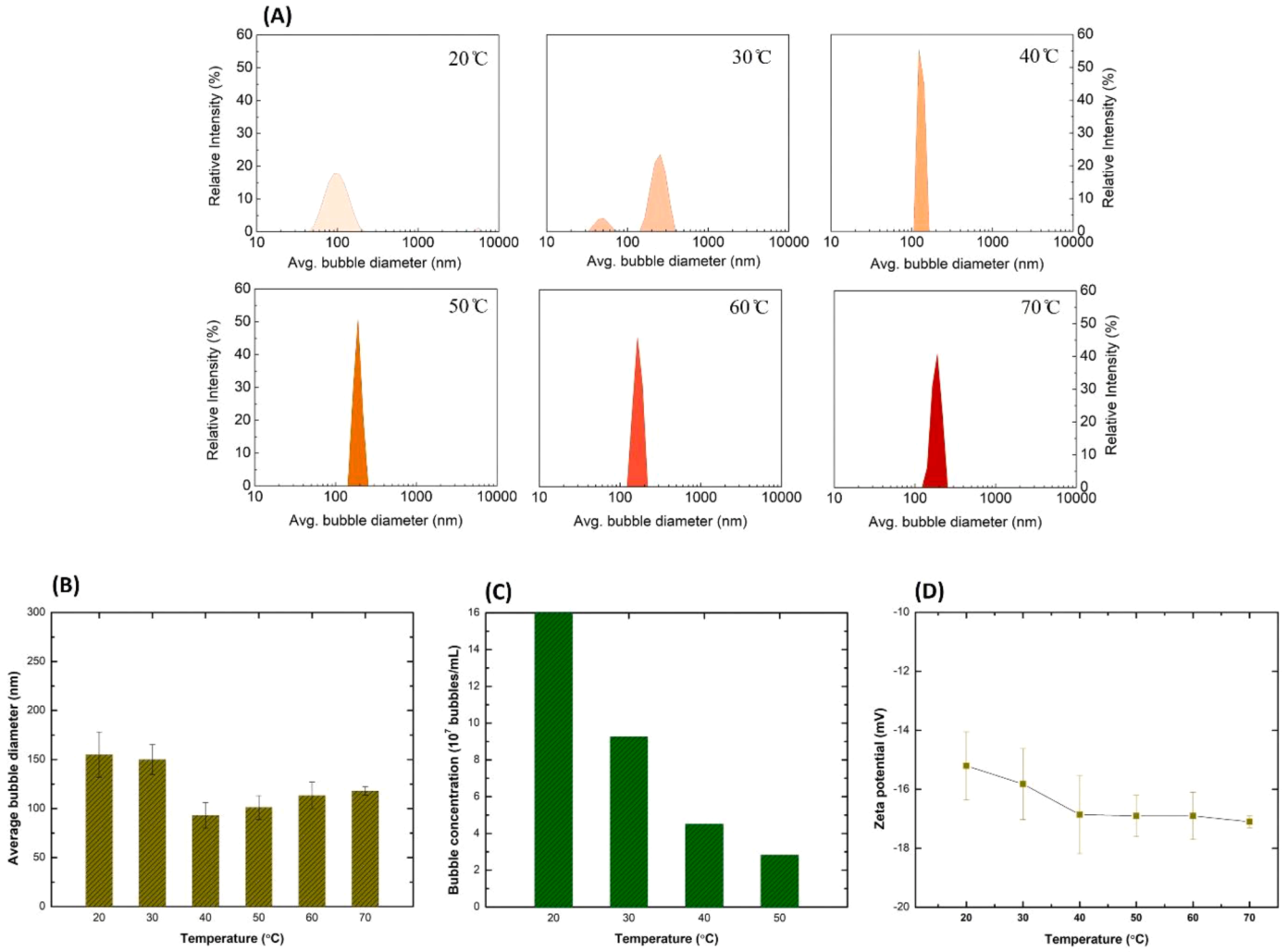

Fig. 3. Effect of temperature on characteristics of nanobubbles in DI water. (A) narrowing of bubble size distribution with increasing temperature from 20 to 70°C, (B) average bubble diameter at a temperature range of 20° to 70°C, (C) concentration of NBs over the 20–50°C temperature range, and (D) changes in zeta potential with various temperatures. Error bars in all figures represent the standard deviation of three measurements in each temperature test.

temperature at which the narrowest size distribution was observed. However, Fig. 3B shows that NBs size increases slowly at temperatures higher than 40°C up to a maximum NBs diameter of 117.92 ± 4.23 nm at 70°C. These observations suggest a transition temperature at around 40 °C where the NBs size shrinks to a minimum upon heating from lower temperatures and steadily expands again upon heating beyond such a transition temperature.

To understand such observations, we first studied the effect of temperature on the concentration of NBs. Fig. 3C shows that within the temperature range tested, the concentration of NBs showed a decreasing trend when temperature increased from 20 to 50°C. The rate of NBs concentration decline, however, was slowing down as the temperature increases at which the highest decrease in NBs concentration was observed when the temperature increased from 20°C to 30°C but slowed after when the temperature increased further up to 40°C and 50°C, respectively. Such a behavior could be due to the coalescence of larger-size bubbles as the temperature increases, followed by their buoyancy and subsequent burst at the surface. In this case, the reminder of NBs is smaller in size and less in concentration which is in line with the measured size in the range of 20°C–40°C (Fig. 3B). However, this does not explain the increase in NBs size associated with the decline in their concentration when the temperature further increased to 50°C. Additionally, our results on the effect of temperature on NBs concentration are contradictory to some of the reported data in literature in which a measurement of NBs concentration as a function of temperature in the range of 20–70°C revealed no change of concentration as a function of temperature and thus concluded that NBs once generated remain stable in the thermal interval tested (20–70°C) (Li et al., 2021). These differences could be attributed to some limitations of the used Nanosight NS300 instrument compared to the Zetasizer NanoZS. For instance, the size range for the Zetasizer (used to measure the size in Fig. 3B: 0.3 nm - 10 μm) is broader than the size range of the NanoSight NS300 (used to measure the concentration in Fig. 3C: 10 nm - 1 μm). Moreover, the concentration range for NanoSight NS300 is limited to 10^6 – 10^9 particles/mL, compared to the Zetasizer NanoZS, which can measure concentrated samples without dilution. However, despite such limitations, it should be noted that although the general trend was a decrease in NBs concentration when the temperature increased (Fig. 3C), the quantitative measurement of NBs concentration still confirms very high numbers of NBs. When the temperature increased up to a maximum of 50°C, the concentration of NBs was around 3×10^7 NBs/mL; a very high concentration that can still contribute to the reduced scaling in MD, as will be discussed in the later sections. Here, and considering such high concentrations of NBs, limitations of the used instrument, and reported literature, we conclude that the generated NBs are deemed to be stable not only over long periods (Fig. 2B and 2C) but also at different temperature changes (Fig. 3C). Yet as mentioned above, the decline in NBs concentration with temperature does not explain the trend in NBs size.

Two temperature ranges have been identified: 20–40°C and 40–70°C being inversely proportional and directly proportional, respectively. Considering the effect of temperature on NBs size and the observed transition trend at around 40°C (Fig. 3B), this suggests that at different temperatures, the NBs either shrink or expand and obtain a new stable equilibrium. Our observations align with the literature, and in a recent study on the stability of bulk NBs over a wide range of temperatures, Li et al. (2021) obtained a similar trend at varying temperatures. Their measurements defined two regimes of size-temperature behavior: a strongly temperature-sensitive regime (10–45°C) where the NBs size shrinks and reaches a minimum, and a weakly temperature-sensitive regime (45–70°C) where the NBs size weakly grow. Upon testing the variation in NBs size from 10 to 70°C and 70–10°C, they found a fully reversible thermodynamic response in this range and concluded stability of NBs. They suggested a correlation between the NBs stability and their negative surface charge. Other recent studies have also suggested that the stability of bulk NBs was due to the selective adsorption of negative electrical charges at the gas-liquid interface of NBs in which bubbles coalescence and diffusion of gas into the bulk liquid are prevented due to the same-charged surface (Nirmalkar et al., 2018b; Tan et al., 2020).

Thus, to test and confirm the negative charge of the NBs interface, we further tested the zeta potential of our NB water via the Zetasizer NanoZS instrument at the same temperature range used to test the bubble size. As expected, NB water showed a negative charge with negative zeta potential values throughout the tested temperature range (Fig. 3D). At around -15.2 ± 3.92 mV at 20°C, the NBs showed increased negativity with increasing the temperature up to 40°C after which the ZP value remained almost constant with further temperature increase up to 70°C. The similarities in a transition temperature (i.e., around 40°C) for the NBs size and ZP show a correlation and confirm the suggestion that the stability of NBs is due to their interface negative charge. Between 20 and 40°C, an increase in the negativity of ZP was associated with a decrease in average NBs size, whereas between 40 and 70°C, an opposite trend was observed (i.e., a slight increase in ZP negativity was associated with a slight increase in average NBs size). Here, the stability of NBs is due to their negative charge at the gas-liquid interface, which is a result of the net amount of hydroxide ions OH^-. This net amount of OH^- results from both adsorbed and desorbed OH^- ions via two competing and temperature-dependent contributors that result in charge stabilization (Li et al., 2021). Higher temperatures promote adsorption of OH^- ions due to increased activity of self-ionization of water, while at the same time promoting desorption of OH^-ions as a result of decreased ions mobility. The sum of these two competing contributors presents the equilibrium OH^- concentration responsible for the negative ZP (i.e., charge) at the liquid-gas interface. At temperatures lower than 40°C, self-ionization of water is slow and the net OH^- is decided by the relatively more dominant OH^- desorption due to ions mobility. However, a significant increase happens for water's self-ionization at temperatures higher than 40°C resulting in higher adsorption of OH^- ions and reaching an equilibrium between the two (i.e., adsorption and desorption), thus showing a relatively stable ZP above 40°C (Fig. 3D) and reaching a new stable equilibrium size (Li et al., 2021).

3.2. Membrane characterization

Because standard hydrophobic membranes' structural and surface properties are fundamental to their performance in MD, we next examined the intrinsic properties of the pristine C-PVDF membrane used in the study. The detailed characteristics of this membrane are presented in Table 2. Briefly, the C-PVDF membrane showed an average pore diameter of 0.22 ± 0.02 μm, with a narrow PSD range of 0.14 ± 0.01 to 0.41 ± 0.03 μm. The surface porosity of the membrane, measured by the gravimetric method, was 65.2 ± 1.52%. The WCA ($123.1° \pm 0.9°$) and LEP (1.88 ± 0.11 bar) of the C-PVDF membrane indicated that the membrane has sufficient hydrophobicity to prevent liquid water transport through it during MD operation. The electric charge on the membrane, as characterized by the negative ZP at neutral pH ($ZP = -39 \pm 0.15$ mV), revealed that the membrane possesses a strong negatively charged surface, which can be attributed to the electronegative charge of the CF moiety in the PVDF polymer (Guo et al., 2018). Similar findings of strong negative charge with negative ZP for the commercial PVDF membranes are reported in the literature (Boo et al., 2016; Chen et al., 2017; Han et al., 2011).

Table 2
Characteristics of the C-PVDF membrane used in the study.

Membrane property	Value
MPS (μm)	0.22 ± 0.02
BP (μm)	0.41 ± 0.03
Minimum PS (μm)	0.14 ± 0.01
Porosity (%)	65.2 ± 1.52
Thickness (μm)	121 ± 0.9
WCA (°)	123.1 ± 0.9
LEP (bar)	1.88 ± 0.11
Zeta potential (mV)*	-39 ± 0.15

* at neutral pH.

3.3. Effect of nanobubbles in deionized water feed on membrane distillation

The first set of experiments was designed to test the effect of introducing NBs to the feed and how the membrane behaves in DCMD without any salt, which was realized by using DI water as the feed either with or without NBs. Such a preliminary test was conducted to eliminate the effect of membrane scaling in the experiment involving NBs in the feed. Fig. 4 shows the DCMD performance, in terms of permeate flux and permeate conductivity, over a 3.5 h period.

The results showed that the C-PVDF membrane did not exhibit any reduction in permeate flux regardless of whether NBs were present in the DI water feed, which was expected given the absence of any foulants or scalants in the feed. However, when tested with the feed containing NBs, the C-PVDF membrane showed slightly higher (7.6%) permeate flux than that in the feed without NBs. This higher flux, although not significant, could be attributable to the hydrodynamic disturbance in the boundary layer when NBs are present in the feed. NBs near the membrane surface can induce turbulence and disturb the boundary layer leading to improved heat transfer transport efficiency and thus mitigation of temperature and concentration polarization effects (Khayet and Matsuura, 2011). The reduction in temperature polarization (TP) enhances the cross-membrane temperature difference (ΔT), resulting in increased vapor flux. However, it should be pointed out that a reduction in TP and the subsequent enhancement of cross-membrane ΔT can also lead to an increased heat loss by conduction resulting in a slight decline in flux. Yet, this decline in flux due to increased heat loss by conduction is expected to be minimal given its weak effect (relative to the more dominant heat transfer through the feed boundary layer, which is maximized in our NBs-enhanced operation as a result of reduced TP) (Khayet and Matsuura, 2011).

Another factor potentially contributing to the increase in flux could be a reduced heat of vaporization of water containing NBs. When NBs are generated in the DI water feed, part of the intermolecular forces that hold the molecules together are broken, reducing the heat of vaporization. This weakening of intermolecular forces increases the surface area of the free water molecules, which means that at the same feed temperature, the vaporization rate increases, increasing the flux. Additionally, one would also consider the possibility of reduced flux in the presence of non-condensable gases due to a decrease in partial vapor pressure. As will be explained later in the scaling inhibition mechanism (Section 3.6), a simple experiment and calculation revealed that the concentration of dissolved CO_2 in the NB-DI water feed is comparable to that of the control DI water feed, and introducing air NBs does not result in considerable changes in the partial vapor pressure that would result in

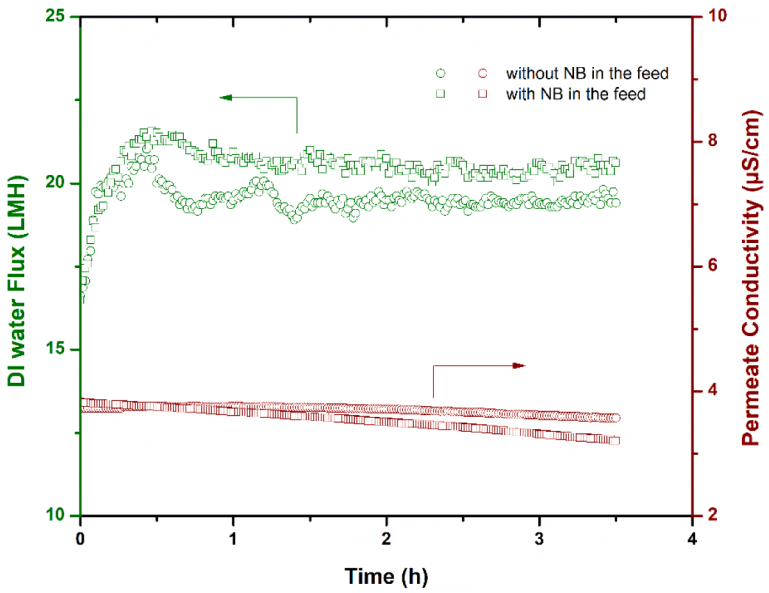

Fig. 4. DCMD performance (water flux and permeate conductivity) of the standard hydrophobic MD (C-PVDF) membrane with deionized (DI) water and NB-DI water as the feeds; the initial stabilized water fluxes of the membrane with these two feeds were 19.4 and 21 L m^{-2} h^{-1}, respectively.

dominant flux reduction.

Overall, while it is difficult to quantify the contribution of each of these factors (i.e., hydrodynamic disturbance in the boundary layer, alleviating TP and CP, increased heat loss by conduction, reduced heat of vaporization, presence of non-condensable gases) on flux, it is concluded from the obtained higher flux that the factors enhancing the flux due to the addition of air NBs into the feed have a more dominant effect than the factors possibly decreasing the flux, and determining the contribution of each mechanism is complex and requires further investigation.

In both tests, permeate conductivity decreased from an initial value of approximately 3.75 μS/cm to 3.57 and 3.20 μS/cm for the feeds without and with NBs, respectively. This reduction is due to the continuous dilution of the permeate by the collected pure water permeate. Here, we also tested the effect of introducing air NBs on the conductivity and pH of the feed. Two feed samples: DI water and NB-DI water, were analyzed for their pH and conductivity, and the measurements showed that upon generating air NBs in DI water for 15 min, both the conductivity and pH remained almost unchanged. In particular, DI water and NB-DI water samples had conductivity values of 4.21 ± 0.32 and 4.15 ± 0.28 μS/cm, and pH values of 6.83 ± 0.14 and 6.71 ± 0.21, respectively.

3.4. *Effect of nanobubbles in high-salinity feed on scaling inhibition in MD*

In this set of experiments, the effect of NBs on membrane scaling during DCMD was evaluated using a high-salinity feed (i.e., HS-100) mimicking RO brine and other hypersaline wastewaters. The feed was

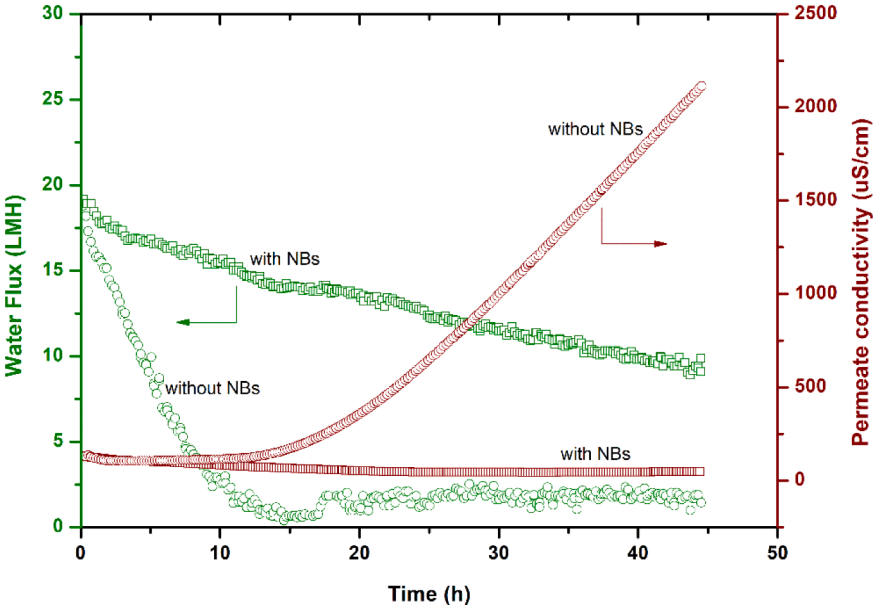

Fig. 5. Scaling behavior (water flux and permeate conductivity) of the C-PVDF membrane in DCMD experiments with a synthetic high-salinity mixture (HS-100) in DI water and HS-100 in NB-DI water as the feeds; the initially stabilized water fluxes of the membrane with these two feeds were 18.8 and 19.2 L m^{-2} h^{-1}, respectively. The experiment ran in a continuous mode without feed replenishment.

prepared by dissolving a mixture of salts (i.e., NaCl, $MgSO_4$, $NaHCO_3$, and $CaCl_2{\cdot}2H_2O$) in DI water to a final concentration of 100 g/L. These salts are usually present in RO brines and other industrial wastewater streams and may lead to severe scaling in MD (Yin et al., 2020). The final ion composition of HS-100 is presented in Table 1.

The results of the two DCMD experiments with the C-PVDF membrane are presented in Fig. 5; the two experiments were conducted under the same conditions but using different feeds: HS-100 in DI water and HS-100 in NB-DI water. Table 3 summarizes the flux trends in the two tests at different points in time. Fig. 5 shows a dramatic decline in the C-PVDF flux in the absence of NBs (i.e., in the HS-100 feed); this decline can be attributed to the combined effect of concentration polarization and severe membrane scaling arising from the precipitation of salts on the membrane surface, followed by crystal growth (Christie et al., 2020). The salt crystals' precipitation and growth block the membrane pores, diminishing the porous area available for vapor transport and creating additional mass and heat transfer resistance (Gryta, 2008b; Rezaei et al., 2020). Consequently, the membrane flux eventually fell from its initial value of 18.8 L m^{-2} h^{-1} to zero (i.e., 100% reduction) after 13 h of MD operation, yielding an average fouling rate (i.e., percentage of flux decline per hour) of 7.69% h^{-1}. For the first 13 h of operation, the membrane did not show signs of wetting, apart from the slight reduction in permeate conductivity due to the pure water permeate; however, after 13 h, the permeate conductivity rapidly increased, indicating membrane wetting.Gryta (2005) demonstrated that scalant deposition on the membrane surface is one of the major reasons for membrane wetting. Yin et al. (2020) tested membranes with different wettability in DCMD using high-salinity feeds and reported that the wetting of PVDF membranes was associated with gypsum scaling. Additionally, the increase in permeate conductivity after 13 h was associated with a slight rise in flux (≈1.8 L m^{-2} h^{-1}), which can be attributed to the passage of the liquid feed, thus confirming the wetting of the C-PVDF membrane, not to be mistaken with pure water vapor flux.

The addition of NBs to the HS-100 feed substantially hindered the flux reduction (Fig. 5), allowing the C-PVDF membrane to be operated for a remarkably prolonged period. In contrast to the DCMD test with HS-100 in DI water as the feed, in which the C-PVDF membrane flux reduced to zero after 13 h, introducing NBs to the feed resulted in a high membrane flux of 14.5 L m^{-2} h^{-1}, a reduction of only 24% from its initial value (19.2 L m^{-2} h^{-1}), with an average fouling rate of 1.88. The decrease in the flux of the C-PVDF membrane in both experiments (with HS-100 in DI water and HS-100 in NB-DI water as the feeds) indicates membrane scaling, but this was more severe in the absence of NBs. After 45 h of operation, the C-PVDF membrane tested with the HS-100 in NB-DI water feed showed a high flux of 9.5 L m^{-2} h^{-1}, a 50% reduction from its initial value, with an average fouling rate of 1.12 (Table 3). Compared with the use of HS-100 in DI water as the feed, this much lower fouling rate and relatively high flux are mainly attributable to the reduced deposition of scalants on the membrane surface. Because the only difference between the feeds was the introduction of the NBs, this reduction in scaling deposition can be concluded to be a direct effect of the NBs. The use of NBs prolonged the life of the C-PVDF membrane, reducing the membrane cleaning and replacement requirements and thereby decreasing the operational costs. The presence of tiny NBs in high concentrations in both the bulk and the boundary layer of the feed enhanced the flow hydrodynamics, which induced turbulence and introduced shear forces near the membrane surface, thus reducing the ability of the salts to deposit and grow.

Moreover, the presence of these air NBs near the feed boundary layer reduced heat losses and minimized the effect of concentration polarization. The detailed mechanism of flux enhancement and scaling reduction in MD due to NBs is explained in detail in the following section. In addition to the improved scaling resistance, the C-PVDF membrane tested with HS-100 in NB-DI water feed did not show any wetting even after 45 h of operation, as evidenced by its stable SR. The permeate conductivity gradually declined throughout the experiment, proving that pure product water was permeating into and diluting the distillate in the distillate tank (Fig. 5). Yin et al. (2020) showed that only a superhydrophobic membrane has excellent resistance against membrane pore wetting associated with gypsum scaling in DCMD, which is due to the membrane's ability to prevent feedwater intrusion into the membrane pores; in contrast, hydrophobic and surface-hydrophilic Janus membranes were both wetted due to severe scaling. In this study, we eliminated the need for complex and expensive modification steps in the fabrication of superhydrophobic membranes; that is, the simple and chemical-free method of introducing NBs into the feed significantly delayed the extend of flux reduction associated with scaling while maintaining robust resistance against the pore wetting of hydrophobic membranes.

The deposition of salts on the membrane surface and the subsequent decline in flux was further evaluated by SEM of the membranes after their use in DCMD (Fig. 6). When the C-PVDF membrane was tested with the HS-100 in DI water feed, a clear and thick salt deposition layer formed on the membrane surface (Fig. 6A1–A3). The whole surface was densely covered, and no pores could be seen, which explains the sharp reduction in flux. However, when NBs were introduced into the feed, salt deposition on the C-PVDF sharply decreased; the surface remained relatively clean, with clear and open pores and only a few crystals (Fig. 6B1–B3). This finding explains the low flux reduction rate of the membrane and its ability to maintain a high flux of 9.5 L m^{-2} h^{-1} after 45 h. Next, the elemental composition of the salt crystals deposited on the membrane surface was identified by EDS of the tested membranes. Two distinct depositions were identified on the surface of the C-PVDF membrane tested with the HS-100 in DI water feed (Fig. 7A1–A6). The spectrum in Fig. 7A2, which corresponds to the C-PVDF surface shown in Fig.71, contains signatures of $CaCl_2$, $CaSO_4$, and NaCl deposits, whereas the spectrum in Fig. 7A5, which corresponds to the C-PVDF surface shown in Fig. 7A4, contains signatures of $CaCl_2$ and NaCl deposits. The mass fraction (wt.%) of the elements found on the membrane surface in both locations (Fig. 7A3 and A6) indicates the presence of low concentrations of the chemical element fluorine (F) of the PVDF membrane material (0.13 and 0.0 wt.%, respectively), proving that the surface pores were blocked entirely. All the salt deposits identified in this study have frequently been reported in the literature as inorganic foulants on MD membranes (Guillen-Burrieza et al., 2013; Kharraz et al., 2015; Warsinger et al., 2015).

In contrast, when tested with the HS-100 in NB-DI water feed, the C-PVDF membrane showed little salt deposition and scaling. The spectrum in Fig. 7A8, which corresponds to the C-PVDF surface shown in Fig. 7A7, has signatures of small deposits of NaCl and $CaCl_2$. The C-PVDF surface was clean and had open pores, as confirmed by the high mass fractions of the chemical elements fluorine and carbon representing the PVDF material (Fig. 7A9). However, it should be pointed out that the EDS technology still faces some limitations that should be considered when used for quantitative analysis. For instance, the detection limit in EDS depends on sample surface conditions and EDS falls short for detection of

Table 3
Trends in flux changes and fouling rates of the C-PVDF membrane.

Feed	Feed/permeate temperature (°C)	Initial flux (L m^{-2} h^{-1})	Final flux (L m^{-2} h^{-1})	Experiment time (h)	Avg. fouling rate (% flux decline/h)
HS-100 without NBs	60/20	18.8	0	13	7.69
HS-100 with NBs	60/20	19.2	14.5	13	1.88
HS-100 with NBs	60/20	19.2	9.5	45	1.12

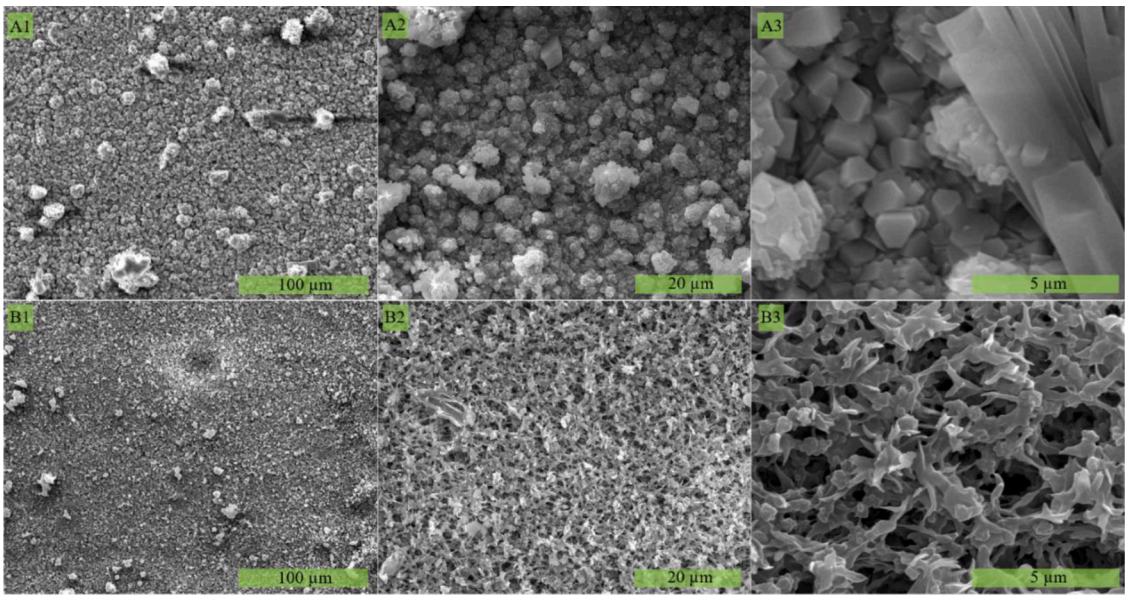

Fig. 6. Scaling behavior and salt deposition: scanning electron microscopy (SEM) images of the C-PVDF membrane after DCMD experiments with the HS-100 in DI water feed (A1–A3) and the HS-100 in NB-DI water feed (B1–B3).

trace elements with concentrations below 1 wt.% (Nasrazadani and Hassani, 2016). Additionally, many software systems used for element identification are vulnerable to the occasional misidentification of major constituent peaks, particularly for minor and trace elements (Newbury and Ritchie, 2013). Thus, although EDS can identify and quantify elements with relatively high accuracy and precision, analysis of EDS data should be performed with caution. Here, the spectra and mass fractions are shown in Fig. 7A corresponds to significant salt deposits detected on the surface of the membrane. Their presence is to compare the blockage and cleanliness of the membrane's surfaces tested with DI water, and NB-DI water feeds, respectively, and as supporting evidence for the SEM images and MD performance but should not be considered statistically representative of the whole membrane surface.

The PSDs of the scaled C-PVDF after DCMD experiments with both feeds and the pristine C-PVDF are shown in Fig. 7B. When tested with different feeds, the scaling propensity of the membranes affected their PSD differently. With the HS-100 in DI water feed, C-PVDF showed a smaller MPS (0.11 ± 0.03 µm), and the PSD shifted toward the smaller sizes, unlike the wide PSD and large MPS of 0.22 ± 0.02 µm of the pristine membrane. This change in pore size is directly related to forming a thick scaling layer on the membrane surface, resulting in partial pore blockage and potential scale intrusion into larger pores, as confirmed by the SEM images. With the HS-100 in NB-DI water feed, however, the C-PVDF membrane showed a different trend in its pore size after DCMD testing, with only a few pores blocked and most of the membrane surface appearing clean with open pores (Fig. 6B1–B3). The MPS was 0.21 ± 0.03 µm, almost identical to the pristine membrane before MD testing, confirming that NBs in the feed imparted the membrane with high resistance against scaling.

Finally, membrane scaling was further confirmed by measuring the water CA, as shown in Fig. 7C. While the pristine C-PVDF membrane showed high hydrophobicity, with a WCA of $123.1^\circ \pm 1.2^\circ$, the membrane tested with the HS-100 in DI water feed for 45 h had a hydrophilic surface, with a WCA as low as $20.5^\circ \pm 3.4^\circ$ This low WCA is due to forming a thick scaling layer on the membrane surface, which increases its affinity for water. HOWEVER, the C-PVDF membrane tested with the HS-100 in NB-DI water feed sustained its hydrophobic nature, with a high WCA of $106.9^\circ \pm 2.2^\circ$, comparable with that of the pristine membrane. Although the reduction in WCA is a sign of scaling in both membranes, the extent of scaling was much lower in the membrane tested with the feed containing NBs, confirming that NBs increase scaling resistance. The results mentioned above, namely the DCMD performance data and the SEM, EDS, PSD, and WCA measurements, all highlight the benefits of introducing air NBs into the feed for improving membrane scaling resistance when treating high-salinity feeds. This chemical-free and straightforward approach extends the operational life of the membranes and reduces the membrane cleaning and replacement costs arising from severe fouling. The benefits of NBs in long-term DCMD testing are discussed in the next section.

3.5. *Long-Term scaling performance of nanobubble-membrane distillation in treating high-salinity feeds*

The experiments discussed thus far revealed that the presence of NBs in feed water was highly effective in delaying membrane scaling during MD operation. However, the effectiveness of NBs in long-term operations is a crucial indicator of MD practicality (Kharraz and An, 2019). Because NBs exhibit high stability and longevity in water, we hypothesized that their persistence in the feed water throughout the test would prevent scale formation and deposition on the C-PVDF membrane surface. To confirm this hypothesis, we have performed an additional experiment to test the performance efficacy of the hybrid NB-MD process in scaling control during high-salinity brine treatment (HS-100) over four consecutive days. Due to the long period of this experiment, the test ran in a batch mode in which the feed was continuously replenished when necessary to keep the variation in feed concentration within 5%.

Fig. 8 presents the distillate flux behavior and SR (%) of the C-PVDF membrane as a function of MD operation time. As illustrated in the figure, the distillate flux of HS-100 in NB-DI water gradually declined throughout the MD operation, reaching a 63% reduction during 98 h testing. In contrast, a high SR (~99.9%) was recorded throughout the test, confirming that the C-PVDF membrane did not experience any wetting even during extended MD operation. We note that when the HS-100 in DI water feed was used, precipitous declines in the distillate flux and SR were recorded only after 13 h of continuous MD operation (Fig. 5). Thus, the observed performance improvement in long-term MD when the HS-100 in NB-DI water feed was used can be directly attributed to the presence of ultrafine NBs in the feed. The steady flux decline and stable high SR during the long-term MD test further verify the effectiveness of NBs in alleviating membrane scaling and consequent wetting during MD operations. In conclusion, although NBs did not completely

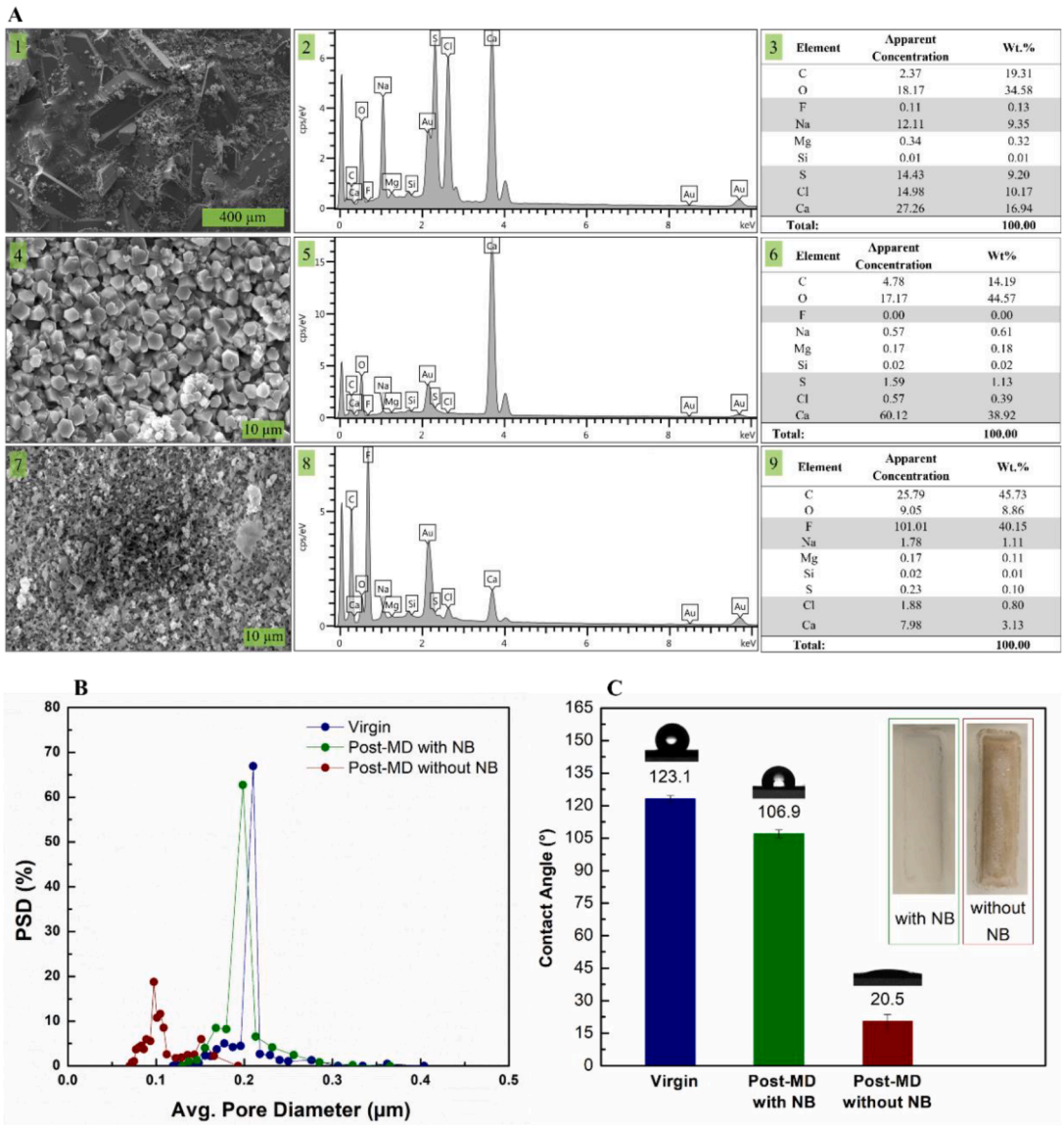

Fig. 7. (A) SEM images of salt depositions on the surface of the C-PVDF membrane when tested with the HS-100 in DI water feed (1 and 4) and with the HS-100 in NB-DI water feed (7) and their corresponding EDS spectra (2,5,8) and a mass fraction (wt.%) of the elements detected on the surface (3,6,9). (B) Effect of scaling on the membrane's pore structure: PSD of the pristine and post-MD C-PVDF membranes tested with HS-100 in DI water and HS-100 in NB-DI water feeds. (C) Wetting characteristics (i.e., the contact angle with DI water) of the pristine and post-MD C-PVDF membranes tested with HS-100 in DI water and HS-100 in NB-DI water feeds. Insets in (C) represent images of the fouled membranes after DCMD testing with HS-100 in DI water and HS-100 in NB-DI water.

prevent the reduction in distillate flux during the long-term MD treatment of a highly saline feed, they significantly prolonged the operational life of the membrane, delaying scaling-induced membrane wetting (details of the scaling control and inhibition mechanisms of NBs in MD are presented in Section 3.6).

3.6. *Scaling inhibition mechanism*

Here we attribute the anti-scaling behavior of NBs to the improved hydrodynamic flow conditions in the feed stream and the adsorption of positive counterions at the negative air-water interface. As discussed in Section 3.1, air NBs have low buoyancy and a strongly negative surface charge, enabling them to remain suspended in water for prolonged periods. In particular, owing to their minimal buoyancy, NBs are subject to Brownian motion and, thus, disperse randomly throughout the feed. At the same time, their negative surface charge (Fig. 3D) ensures that the millions of NBs in each milliliter of the solution repel each other, thus wholly saturating the feed stream and realizing homogenous mixing. Specifically, the exceptionally high concentration of continually moving NBs induces turbulent flow in the feed channel, producing uniform flow circulation, and thus, increasing the surface shear forces at the membrane surface and improving local mixing in the feed stream. The surface shear rate directly influences the heat and mass transfer coefficients in the feed stream (Chen et al., 2014; Olatunji and Camacho, 2018). The high shear stress acting on the membrane surface creates a physical disturbance in the boundary layer, increasing the heat and mass transfer coefficients (Chen et al., 2014; Wu et al., 2015). The high heat transfer coefficient increases the temperature at the membrane surface, whereas the high mass transfer coefficient decreases the salt ion concentration at the membrane surface, respectively alleviating temperature, and concentration polarization effects during MD operation. These improved hydrodynamic conditions in the feed stream induced by NBs play an essential role in delaying scale formation and deposition on the membrane surface.

In addition to NB-induced shear stress on the membrane surface, the electrostatic attraction of the counterions to the negatively charged NBs

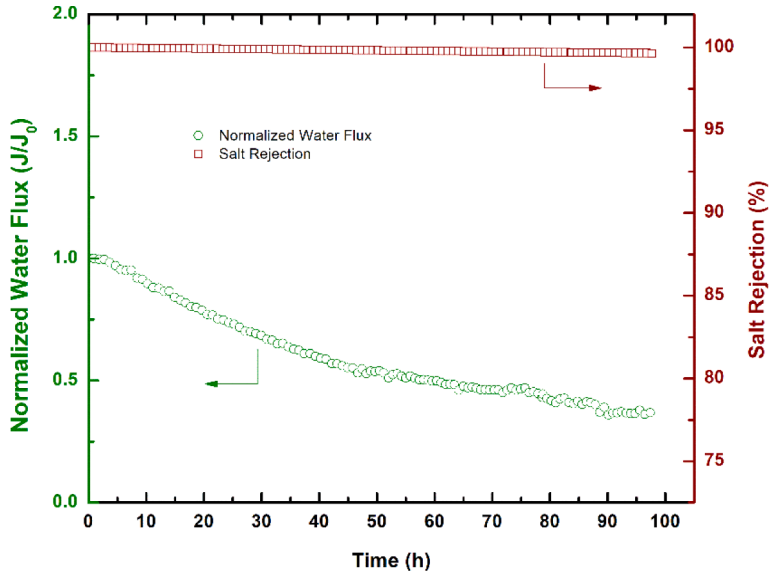

Fig. 8. Scaling behavior (normalized water flux and salt rejection) of the C-PVDF membrane in long-term DCMD with HS-100 in NB-DI water feed. The experiment ran in a batch mode where the feed was replenished with DI water whenever 100 mL permeate was collected to keep the variation in feed concentration within 5%.

also contributes to the scale inhibition performance of the NB-MD system. Briefly, as aforementioned, the produced NBs carry high negative zeta potential, owing to the excess of hydroxide ions (OH^-) compared to hydrogen ions (H^+) at the gas-water interface, mainly due to the difference in enthalpies of hydration. The hydration energy of OH^- (−489 kJ/mol) is much lower than that of H^+ (−1127 kJ/mol), which means that OH^- is more inclined to stay at the gas-water interface giving a negative charge to the bubbles. Moreover, the orientation of water dipoles at the interface may also determine the interface charge, with hydrogen atoms pointing toward the water phase and oxygen atoms toward the gas phase, causing an attraction of anions to the interface. These adsorbed OH^- and H^+ ions are crucial factors that influence the interface charge, while other electrolyte ions are attracted to the interface, as the counterions, by electrostatic forces. For instance, here, the NBs with negatively charged interface accumulates/attracts the positively charged ions from the feed stream (Na^+, Ca^{2+}, Mg^{2+}, etc.) to preserve electrical neutrality and, consequently, form an electric double layer (Eq. (1a)).

$$NB - OH^- \ldots + \text{ionsinfeed} \leftrightarrow NB - OH^- ion^{2+} \ldots \quad (1a)$$

The force of attraction between the NB interface and the ions is highly dependent on the valency of the counterions (Bui et al., 2019; Takahashi, 2005). For instance, ions with a valency of +2 (e.g., Ca^{2+} and Mg^{2+}) tend to have a stronger affinity for the air-water interface than do monovalent ions (e.g., Na^+) due to static electricity (Takahashi, 2005). Moreover, it is also well-established that in MD, salts of calcium and magnesium have a much higher membrane scaling potential than salts of sodium (Kharraz et al., 2015; Warsinger et al., 2015). Given their large specific surface area and negative surface charge, NBs in the saline feed attract positive ions, with a higher affinity for divalent Ca^{2+} and Mg^{2+} ions than for monovalent Na^+ ions. This effect significantly reduces the availability of Ca^{2+} and Mg^{2+} in the bulk feed for scale formation, thereby improving the long-term performance efficacy of NB-assisted MD in the treatment of high-salinity water (Fig. 8).

Moreover, one can think that the presence of NBs in the feed may affect the CO_2 concentration or alter the CO_2/carbonates equilibrium thus, contributing to the observed lower scaling for the NBs containing feed. To test this possibility, we have performed a simple experiment to measure the concentration of dissolved CO_2 in two samples: a control DI water and NBs-DI water (the experimental procedure is given under Section 2.2). We found that generating NBs does not highly affect the dissolved CO_2 concentration. The NBs-DI water sample had a CO_2 concentration comparable to that found in the control DI water sample. In fact, both samples had shown to have a minimal amount of dissolved CO_2 (less than 1 mg/L – the real concentration is expected to be even lower since only one droplet of the titrant NaOH was enough to complete the reaction). This is expected since the NBs used in this study were generated in air, in which CO_2 represents less than 0.03% of the air volume (Buis, 2019), and thus, the concentration of CO_2 in the generated NBs is very low. We, therefore, concluded that changes in CO_2/carbonate equilibrium due to the generation of NBs are not expected to contribute much to the scaling behavior of the C-PVDF membrane during MD, compared to the more dominant surface shear force and NBs charge effect, as explained earlier.

4. Conclusions

Membrane scaling represents a significant challenge hindering MD industrial application, especially for treating hypersaline wastewaters and brine recovery and reduction. This study demonstrated the benefits of introducing air nanobubbles into the feed, as a chemical-free and straightforward method, for alleviating flux reduction and membrane pore wetting associated with mineral scaling in MD. A commercial PVDF membrane was challenged with high-salinity brine feed either with the absence or introduction of NBs in a DCMD system. Compared to the high salinity in DI water feed, introducing NBs reduced membrane scaling propensity and offered excellent resistance against pore wetting associated with scaling. While the membrane surface tested with NBs in the feed showed minimal flux reduction (63% after long-term 98 h) without the occurrence of pore wetting, the membrane tested without NBs in the feed experienced severe scaling and complete loss of flux reaching zero within 13 h of operation, after which membrane pore wetting was detected. SEM images of the fouled membranes revealed an accumulation of salts crystals blocking the membrane pores and a formation of thick salts layer on the surface of the membrane tested without NBs in the feed, compared to a clean surface with open pores and significantly fewer salts deposition for the membrane tested with NBs in the feed. Additionally, EDS elemental analysis and PSDs and CAs of the pristine and fouled membranes samples confirmed the presence of severe $CaSO_4$, $MgSO_4$, and $CaCl_2$ crystals growth resulting in reduced pore sizes and loss of surface hydrophobicity when NBs were absent in the high-salinity feed. We attribute the improved scaling resistance and absence of pore

wetting associated with introducing NBs into the feed to a combination of mechanisms, including high surface shear forces due to flow turbulence and electrostatic attractions between the negatively-charged NBs and the counterions. Our findings demonstrate the advantage of introducing NBs into the feed for MD treatment of challenging hypersaline feeds and offer valuable insights for the future development of simple, chemical-free strategies for inorganic scaling control in MD.

Declaration of Competing Interest

The authors declare that they have no known competing financial interests or personal relationships that could have appeared to influence the work reported in this paper.

Acknowledgments

This work was supported by the Research Grant Council of Hong Kong through Theme-based Research Scheme (Project No. [T21–604/19-R]), Enviromental Conservation Fund (ECF 05/2020), Marine Conservation Enhancement Fund (MCEF20017), and UK Government – Department of Health and Social Care (DHSC), Global AMR Innovation Fund (GAMRIF), and the International Development Research centre (IDRC), Ottawa, Canada (grant #109050–001). The views expressed herein do not necessarily represent those of IDRC or its Board of Governors.

The authors would like to acknowlege AquaPro Solutions as Industry Collaborator for providing nanobubble Generator technology and field deployment knowhow for research project.

References

Agarwal, A., Ng, W.J., Liu, Y., 2011. Principle and applications of microbubble and nanobubble technology for water treatment. Chemosphere 84, 1175–1180. https://doi.org/10.1016/j.chemosphere.2011.05.054.

Alkhudhiri, A., Darwish, N., Hilal, N., 2012. Membrane distillation: a comprehensive review. Desalination 287, 2–18. https://doi.org/10.1016/j.desal.2011.08.027.

Atkinson, A.J., Apul, O.G., Schneider, O., Garcia-Segura, S., Westerhoff, P., 2019. Nanobubble technologies offer opportunities to improve water treatment. Acc. Chem. Res. https://doi.org/10.1021/acs.accounts.8b00606.

Boo, C., Lee, J., Elimelech, M., 2016. Omniphobic polyvinylidene fluoride (PVDF) membrane for desalination of shale gas produced water by membrane distillation. Environ. Sci. Technol. 50, 12275–12282. https://doi.org/10.1021/acs.est.6b03882.

Bui, T.T., Nguyen, D.C., Han, M., 2019. Average size and zeta potential of nanobubbles in different reagent solutions. J. Nanoparticle Res. 21 https://doi.org/10.1007/s11051-019-4618-y.

Buis, A., 2019. The Atmosphere: Getting a Handle on Carbon Dioxide [WWW Document]. Global Climate Change: Vital Signs of the planet. URL https://climate.nasa.gov/news/2915/the-atmosphere-getting-a-handle-on-carbon-dioxide/ (accessed 11.11.21).

Chen, G., Yang, X., Lu, Y., Wang, R., Fane, A.G., 2014. Heat transfer intensification and scaling mitigation in bubbling-enhanced membrane distillation for brine concentration. J. Memb. Sci. 470, 60–69. https://doi.org/10.1016/j.memsci.2014.07.017.

Chen, G., Yang, X., Wang, R., Fane, A.G., 2013. Performance enhancement and scaling control with gas bubbling in direct contact membrane distillation. Desalination 308, 47–55. https://doi.org/10.1016/j.desal.2012.07.018.

Chen, Y., Tian, M., Li, X., Wang, Y., An, A.K., Fang, J., He, T., 2017. Anti-wetting behavior of negatively charged superhydrophobic PVDF membranes in direct contact membrane distillation of emulsified wastewaters. J. Membr. Sci. 535, 230–238. https://doi.org/10.1016/j.memsci.2017.04.040.

Christie, K.S.S., Yin, Y., Lin, S., Tong, T., 2020. Distinct behaviors between gypsum and silica scaling in membrane distillation. Environ. Sci. Technol. https://doi.org/10.1021/acs.est.9b06023.

Cui, Z.F., Chang, S., Fane, A.G., 2003. The use of gas bubbling to enhance membrane processes. J. Membr. Sci. 221, 1–35. https://doi.org/10.1016/S0376-7388(03)00246-1.

Deka, B.J., Guo, J., Khanzada, N.K., An, A.K., 2019. Omniphobic re-entrant PVDF membrane with ZnO nanoparticles composite for desalination of low surface tension oily seawater. Water Res. 165, 114982 https://doi.org/10.1016/j.watres.2019.114982.

Deshmukh, A., Boo, C., Karanikola, V., Lin, S., Straub, A.P., Tong, T., Warsinger, D.M., Elimelech, M., 2018. Membrane distillation at the water-energy nexus: limits, opportunities, and challenges. Energy Environ. Sci. https://doi.org/10.1039/c8ee00291f.

Ding, Z., Liu, L., Liu, Z., Ma, R., 2011. The use of intermittent gas bubbling to control membrane fouling in concentrating TCM extract by membrane distillation. J. Membr. Sci. 372, 172–181. https://doi.org/10.1016/j.memsci.2011.01.063.

Drioli, E., Ali, A., Macedonio, F., 2015. Membrane distillation: recent developments and perspectives. Desalination 356, 56–84. https://doi.org/10.1016/j.desal.2014.10.028.

Eykens, L., De Sitter, K., Dotremont, C., Pinoy, L., Van der Bruggen, B., 2017. Membrane synthesis for membrane distillation: a review. Sep. Purif. Technol. 182, 36–51. https://doi.org/10.1016/j.seppur.2017.03.035.

Gryta, M., 2008a. Chemical pretreatment of feed water for membrane distillation. Chem. Pap. 62, 100–105. https://doi.org/10.2478/s11696-007-0085-5.

Gryta, M., 2008b. Fouling in direct contact membrane distillation process. J. Membr. Sci. 325, 383–394. https://doi.org/10.1016/j.memsci.2008.08.001.

Gryta, M., 2005. Long-term performance of membrane distillation process. J. Membr. Sci. 265, 153–159. https://doi.org/10.1016/j.memsci.2005.04.049.

Guillen-Burrieza, E., Thomas, R., Mansoor, B., Johnson, D., Hilal, N., Arafat, H., 2013. Effect of dry-out on the fouling of PVDF and PTFE membranes under conditions simulating intermittent seawater membrane distillation (SWMD). J. Membr. Sci. 438, 126–139. https://doi.org/10.1016/j.memsci.2013.03.014.

Guo, J., Farid, M.U., Lee, E.J.J., Yan, D.Y.S.S., Jeong, S., An, A.K., Kyoungjin An, A., 2018. Fouling behavior of negatively charged PVDF membrane in membrane distillation for removal of antibiotics from wastewater. J. Membr. Sci. 551, 12–19. https://doi.org/10.1016/j.memsci.2018.01.016.

Han, M.J., Baroña, G.N.B., Jung, B., 2011. Effect of surface charge on hydrophilically modified poly(vinylidene fluoride) membrane for microfiltration. Desalination 270, 76–83. https://doi.org/10.1016/j.desal.2010.11.024.

He, F., Sirkar, K.K., Gilron, J., 2009. Effects of antiscalants to mitigate membrane scaling by direct contact membrane distillation. J. Membr. Sci. 345, 53–58. https://doi.org/10.1016/j.memsci.2009.08.021.

Horseman, T., Yin, Y., Christie, K.S., Wang, Z., Tong, T., Lin, S., 2021. Wetting, scaling, and fouling in membrane distillation: state-of-the-art insights on fundamental mechanisms and mitigation strategies. ACS EST Eng. 1, 117–140. https://doi.org/10.1021/acsestengg.0c00025.

Kamranvand, F., Davey, C.J., Williams, L., Parker, A., Jiang, Y., Tyrrel, S., McAdam, E.J., 2020. Ultrafiltration pretreatment enhances membrane distillation flux, resilience and permeate quality during water recovery from concentrated blackwater (urine/faeces). Sep. Purif. Technol. 253, 117547 https://doi.org/10.1016/j.seppur.2020.117547.

Kharraz, J.A., An, A.K., 2019. Patterned superhydrophobic polyvinylidene fluoride (PVDF) membranes for membrane distillation: enhanced flux with improved fouling and wetting resistance. J. Membr. Sci. 595, 117596 https://doi.org/10.1016/j.memsci.2019.117596.

Kharraz, J.A., Bilad, M.R., Arafat, H.A., 2015. Flux stabilization in membrane distillation desalination of seawater and brine using corrugated PVDF membranes. J. Membr. Sci. 495, 404–414. https://doi.org/10.1016/j.memsci.2015.08.039.

Kharraz, J.A., Farid, M.U., Khanzada, N.K., Deka, B.J., Arafat, H.A., An, A.K., 2020. Macro-corrugated and nano-patterned hierarchically structured superomniphobic membrane for treatment of low surface tension oily wastewater by membrane distillation. Water Res. 174, 115600 https://doi.org/10.1016/j.watres.2020.115600.

Khayet, M., Matsuura, T., Khayet, M., Matsuura, T., 2011. Chapter 10 - direct contact membrane distillation. Membrane Distillation. Elsevier, Amsterdam, pp. 249–293. https://doi.org/10.1016/b978-0-444-53126-1.10010-7.

Li, M., Ma, X., Eisener, J., Pfeiffer, P., Ohl, C.D., Sun, C., 2021. How bulk nanobubbles are stable over a wide range of temperatures. J. Colloid Interface Sci. 596, 184–198. https://doi.org/10.1016/j.jcis.2021.03.064.

Liu, L., Xiao, Z., Liu, Y., Li, X., Yin, H., Volkov, A., He, T., 2021. Understanding the fouling/scaling resistance of superhydrophobic/omniphobic membranes in membrane distillation. Desalination 499. https://doi.org/10.1016/j.desal.2020.114864.

Lugli, F., Höfinger, S., Zerbetto, F., 2005. The collapse of nanobubbles in water. J. Am. Chem. Soc. 127, 8020–8021. https://doi.org/10.1021/ja0505447.

Malvern Panalytical Ltd., 2021. NanoSight LM10 [WWW Document]. Malvern Panalytical Ltd. URL https://www.malvernpanalytical.com/en/products/product-range/nanosight-range/nanosight-lm10 (accessed 11.1.21).

Meegoda, J.N., Aluthgun Hewage, S., Batagoda, J.H., 2018. Stability of nanobubbles. Environ. Eng. Sci. 35, 1216–1227. https://doi.org/10.1089/ees.2018.0203.

Nasrazadani, S., Hassani, S., 2016. Modern analytical techniques in failure analysis of aerospace, chemical, and oil and gas industries. Handbook of Materials Failure Analysis with Case Studies from the Oil and Gas Industry. Elsevier Inc., pp. 39–54. https://doi.org/10.1016/B978-0-08-100117-2.00010-8

Newbury, D.E., Ritchie, N.W.M., 2013. Is Scanning electron microscopy/energy dispersive X-ray spectrometry (SEM/EDS) quantitative? Scanning 35, 141–168. https://doi.org/10.1002/sca.21041.

Nirmalkar, N., Pacek, A.W., Barigou, M., 2018a. On the existence and stability of bulk nanobubbles. Langmuir 34, 10964–10973. https://doi.org/10.1021/acs.langmuir.8b01163.

Nirmalkar, N., Pacek, A.W., Barigou, M., 2018b. Interpreting the interfacial and colloidal stability of bulk nanobubbles. Soft Matter 14, 9643–9656. https://doi.org/10.1039/c8sm01949e.

Olatunji, S.O., Camacho, L.M., 2018. Heat and mass transport in modeling membrane distillation configurations: a review. Front. Energy Res. 6, 1–18. https://doi.org/10.3389/fenrg.2018.00130.

Pangarkar, B.L., Deshmukh, S.K., Sapkal, V.S., Sapkal, R.S., 2016. Review of membrane distillation process for water purification. Desalin. Water Treat. 57, 2959–2981. https://doi.org/10.1080/19443994.2014.985728.

Rezaei, M., Alsaati, A., Warsinger, D.M., Hell, F., Samhaber, W.M., 2020. Long-running comparison of feed-water scaling in membrane distillation. Membranes 10, 1–21. https://doi.org/10.3390/membranes10080173.

Rezaei, M., Warsinger, D.M., Lienhard, V.J.H., Duke, M.C., Matsuura, T., Samhaber, W. M., 2018. Wetting phenomena in membrane distillation: mechanisms, reversal, and prevention. Water Res. 139, 329–352. https://doi.org/10.1016/j.watres.2018.03.058.

Servi, A.T., Kharraz, J., Klee, D., Notarangelo, K., Eyob, B., Guillen-Burrieza, E., Liu, A., Arafat, H.A., Gleason, K.K., 2016. A systematic study of the impact of hydrophobicity on the wetting of MD membranes. J. Membr. Sci. 520, 850–859. https://doi.org/10.1016/j.memsci.2016.08.021.

Sweity, A., Oren, Y., Ronen, Z., Herzberg, M., 2013. The influence of antiscalants on biofouling of RO membranes in seawater desalination. Water Res. 47, 3389–3398. https://doi.org/10.1016/j.watres.2013.03.042.

Takahashi, M., 2005. ζ Potential of microbubbles in aqueous solutions: electrical properties of the gas - Water interface. J. Phys. Chem. B 109, 21858–21864. https://doi.org/10.1021/jp0445270.

Tan, B.H., An, H., Ohl, C.D., 2020. How bulk nanobubbles might survive. Phys. Rev. Lett. 124, 134503 https://doi.org/10.1103/PhysRevLett.124.134503.

Tijing, L.D., Woo, Y.C., Choi, J.S., Lee, S., Kim, S.H., Shon, H.K., 2015. Fouling and its control in membrane distillation-A review. J. Membr. Sci. 475, 215–244. https://doi.org/10.1016/j.memsci.2014.09.042.

Ullah, R., Khraisheh, M., Esteves, R.J., McLeskey, J.T., AlGhouti, M., Gad-el-Hak, M., Vahedi Tafreshi, H., 2018. Energy efficiency of direct contact membrane distillation. Desalination 433, 56–67. https://doi.org/10.1016/j.desal.2018.01.025.

Ushikubo, F.Y., Furukawa, T., Nakagawa, R., Enari, M., Makino, Y., Kawagoe, Y., Shiina, T., Oshita, S., 2010. Evidence of the existence and the stability of nano-bubbles in water. Colloids Surf. A Physicochem. Eng. Asp. 361, 31–37. https://doi.org/10.1016/j.colsurfa.2010.03.005.

Warsinger, D.M., Swaminathan, J., Guillen-Burrieza, E., Arafat, H.A., Lienhard, V, J.H., 2015. Scaling and fouling in membrane distillation for desalination applications: a review. Desalination 356, 294–313. https://doi.org/10.1016/j.desal.2014.06.031.

Wu, C., Li, Z., Zhang, J., Jia, Y., Gao, Q., Lu, X., 2015. Study on the heat and mass transfer in air-bubbling enhanced vacuum membrane distillation. Desalination 373, 16–26. https://doi.org/10.1016/j.desal.2015.07.001.

Ye, Y., Yu, S., Hou, L., Liu, B., Xia, Q., Liu, G., Li, P., 2019. Microbubble aeration enhances performance of vacuum membrane distillation desalination by alleviating membrane scaling. Water Res. 149, 588–595. https://doi.org/10.1016/j.watres.2018.11.048.

Yin, Y., Jeong, N., Tong, T., 2020. The effects of membrane surface wettability on pore wetting and scaling reversibility associated with mineral scaling in membrane distillation. J. Membr. Sci. 614, 118503 https://doi.org/10.1016/j.memsci.2020.118503.

Zhang, P., Knötig, P., Gray, S., Duke, M., 2015. Scale reduction and cleaning techniques during direct contact membrane distillation of seawater reverse osmosis brine. Desalination 374, 20–30. https://doi.org/10.1016/j.desal.2015.07.005.